半導体人工原子･分子における高周波電子スピン操作

Twente University, Institute for NanoTechnology Research Program Director

Wilfred Gerard van der Wiel

High-frequency electron-spin manipulation in semiconductor artificial atoms and molecules

Wilfred G. van der Wiel

研究のねらい (Objective)

The aim of the project is high-frequency (GHz) electron-spin manipulation in semiconductor few-electron quantum dots. The main motivation of this proposal is formed by the possible application of electron spins as basic building blocks for quantum logic.
One concrete aim is to rotate a single-electron spin in a few-electron quantum by means of a locally generated electron spin resonance (ESR) field. A key experiment that still needs to be done is the determination of the single-electron spin decoherence time T_2 in a semiconductor environment. The next logical step after studying single dots is to look at double dot systems. The entanglement of two electron spins using tunnel-coupled quantum dots is of great importance for the realization of the XOR (or controlled-NOT) gate operation.

研究成果 (Research Results)

1. Few-electron quantum dot devices for single electron spin resonance

Numerous proposals have been advanced for systems that manifest assemblies of "qubits", which can be used to achieve quantum computing [1]. Each such system must demonstrate a variety of properties (long coherence lifetime, initialization ability, readout, etc.), one of the most important of which is the existence of some form of entanglement operation between two qubits. Stimulated by the Loss and DiVincenzo proposal [2], there is a continuing experimental effort to realize electron spin quantum bits, or *qubits*, in semiconductor quantum dots [3]. The qubit consists of the spin-up $|\uparrow\rangle$ and spin-down $|\downarrow\rangle$ of a single electron in a quantum dot. Ideally, although not necessarily, single-electron quantum dots are used. The proposal comprises single-qubit rotations using electron spin resonance (ESR) and two-qubit quantum gates relying on exchange interaction between electrons in a double quantum dot [4]. The XOR (CNOT) 2-qubit gate in combination with arbitrary single-qubit rotations forms a universal set of quantum logic gates. In fact, the CNOT gate combined with arbitrary rotations about two independent axes is already sufficient. After manipulation of the spin degree of freedom, read-out can be realized via spin-to-charge conversion.

In this section, we discuss quantum dot devices with an integrated high-frequency line to generate an ac magnetic field in the vicinity of the quantum dot. This ac magnetic field is intended for realizing single electron spin ESR. The effective g-factor in our GaAs dot is derived and microwave experiments show the importance of photon assisted tunneling (PAT) and pumping.

When a static magnetic field, B_0, is applied, the spin-up state and the spin-down state split by the Zeeman energy $\Delta E_Z = g_{dot}\mu_B B_0$ with g_{dot} the g-factor in the dot and μ_B the Bohr magneton. For g_{dot} = 0.44 (as in bulk GaAs) and B_0 = 5 T, ΔE_z = 0.13 meV. Electron spins precess around the B_0-axis with (Larmor) frequency $f_B = \Delta E_Z / h = g_{dot}\mu_B B_0 / h$. Using the numerical values above, we find $f_B \sim$ 30 GHz. A microwave magnetic field, B_{ac}, in a plane perpendicular to B_0 and in resonance with the precession rate, causes coherent oscillations between the states $|\uparrow\rangle$ and $|\downarrow\rangle$ (electron spin resonance: ESR). The rotation frequency, or Rabi frequency, is proportional to the strength of B_{ac}: $f_{Rabi} = g_{dot}\mu_B B_{ac} / h$. For B_{ac} = 10 mT, $f_{Rabi} \sim$ 60 MHz. The Larmor precession and the B_{ac}-induced Rabi oscillations offer two perpendicular axes of rotation, enabling in principle any desired qubit rotation.

In order to control the spin rotation angle, it is necessary that one can turn on and off the ac magnetic field on short timescales. The typical time for performing half a spin rotation (or π-pulse manipulation) is ~10 ns. This value is much smaller than the expected single-electron spin decoherence time, $T_2 > 1$ μs [5]. To observe single-electron ESR in the quantum dot via an electron transport measurement we follow the proposals of Engel et al. [6,7] or slight variations on them. By properly tuning the voltages applied to the dot, electron transport can be turned on and off via an ESR field. As outlined in Refs. [6,7], one can derive (a lower bound of) T_2 from the ESR-related current through the dot. It is more appropriate to talk about T_2^* (pronounced as T-2-star), where the asterisk refers to an ensemble average. Although single electron spin resonance is considered, a repetition of the experiment is required to obtain a measurable current. Thus, an ensemble average (in time domain) is measured. A measurement of the (non-averaged) value of T_2 would require single-shot read-out [8] or spin-echo pulse sequences to suppress dephasing [5].

Since g_{dot} is expected to differ significantly from the value in bulk GaAs (e.g. due to the effect of confinement and the "leakage" of the electron wavefunction in the AlGaAs barriers), we first independently determine g_{dot}, as discussed in section 4.1.2. We discuss our microwave results in section 4.1.3, in particular the influence of the (undesired) ac electric field at the site of the dot.

1.1. Device layout

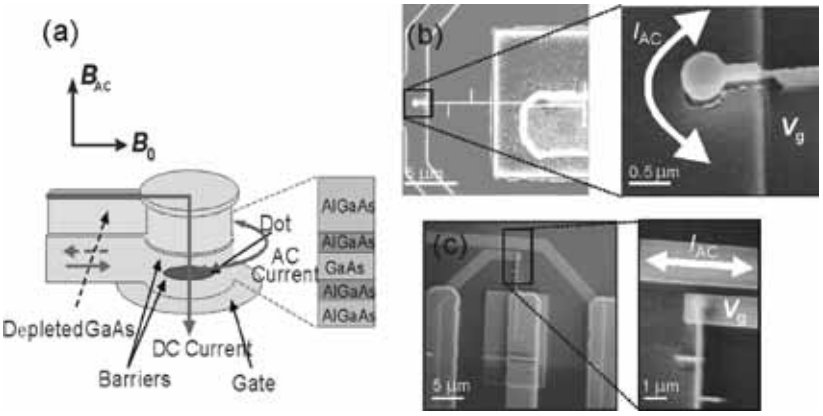

FIGURE 1. (a) Schematic of a vertical quantum dot (VQD) with a ring gate used for generating an ac magnetic field B_{ac}. The device is positioned in a static magnetic field B_0 parallel to the dot plane. (b) Scanning electron microscope (SEM) pictures of a VQD device with a local ac magnetic field generator. In the "combination type" a Ti/Au gate electrode is used for applying both a DC voltage and an ac current. (c) SEM pictures of a VQD device with a separate local ac magnetic field generator. In the "separate wire type" a Ti/Au wire is fabricated in the vicinity (~1 µm) *of the dot.*

The device is formed out of a GaAs/AlGaAs double barrier structure (Fig. 1). In contrast to previous devices [9] we do not include a small concentration of In in the GaAs quantum well, which reduces the lattice strain. A narrow, so-called mesa bridge supports the lead to the top contact. This mesa bridge is so narrow (< 0.15 µm) that no parasitic current can flow between the top and back contact. In order to locally manipulate an electron spin in the dot, a local and time controllable ESR source is needed. The approach is to apply a high-frequency current to a metal strip line near the dot in order to generate a local ac magnetic field. Here, we discuss two types of devices designed for creating such an ac field, which we call the "combination type" and the "separate wire type". In the combination type, B_{ac} is generated by driving an ac current through the Ti/Au ring gate wrapped around the dot, which is at the same time used to squeeze the effective dot size by applying a negative dc voltage (Fig. 1a,b). Thus, the ac magnetic field is perpendicular to the dot. A ~mA current is required to generate a magnetic field of ~mT at the site of the dot. In the separate wire type, B_{ac} is generated by driving an ac current through a separate Ti/Au line nearby the dot (Fig.1c). Also here, a ~mT field requires a ~mA current. The advantage of the combination type is that the distance between the dot and ac line is as small as possible, thereby minimizing the required ac current for a given ac magnetic field. On the other hand, the separation type is experimentally easier to implement and

may be more advantageous as far as local heating and capacitive coupling to the dot are concerned. We use semi-rigid and flexible coax cables to bring the microwave signal (generated at room temperature, 10 MHz–50 GHz) to the sample holder in which the coax line is connected to the on-chip ac line via a 50 Ω impedance matched coplanar waveguide and short (~3 mm) Au bonding wires. The length of the bonding wires should be short in comparison to the microwave wavelength (λ = 3 cm for 10 GHz). The dc resistance of the on-chip ac line is ~20 Ω. In order to reduce the shunt electrostatic coupling between the ac line and the dot, we remove redundant parts of the n-doped layer down to the semi-insulating GaAs substrate [10].

1.2. Determination of g-factor in GaAs vertical quantum dots

All experimental results presented below are obtained in "separate wire" devices in a dilution refrigerator with a base temperature of 70 mK. A static magnetic field B_0 is applied to the dot in the parallel configuration (see Fig. 1a). This magnetic field configuration allows resolving the Zeeman splitting while minimizing the effect of the magnetic field on the orbital (Fock-Darwin) states.

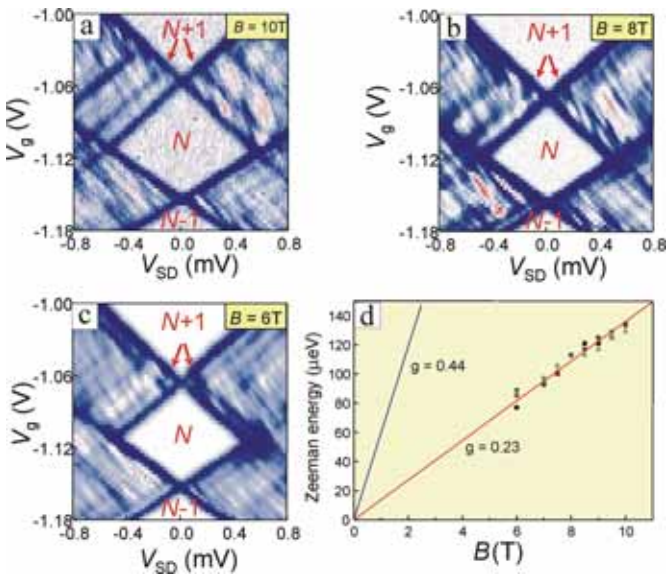

FIGURE 2. Plots of the differential conductance dI/dV vs. gate voltage V_g and source-drain voltage V_{sd} for three different parallel magnetic fields, B = 10 T (a), 8 T (b), and 6 T (c). The B-evolution of a Zeeman split state (indicated by arrows) is clearly observed. (d) Zeeman energy as a function of B. The Zeeman energy cannot be resolved for B < 6 T. From the linear fit to the data (red line) $|g_{dot}|$ = 0.23 ± 0.02 is derived. The Zeeman energy in bulk GaAs ($|g_{GaAs}|$ = 0.44) is plotted for comparison. The different symbols correspond to different positions in the Coulomb diamond where the Zeeman splitting has been evaluated.

Figure 2 shows the differential conductance dI/dV versus gate voltage V_g and source drain voltage V_{sd} measured for three different in-plane magnetic fields. A white diamond shaped region in the center indicates Coulomb blockade for N ~ 20 electrons. Due to leakage between the gate and source contacts for gate voltages below −3 V, we are not able to reduce the electron number to one. Electron numbers down to zero have been achieved for devices in the same fabrication run though. This Coulomb blockade region is bounded by four lines indicating alignment between one of the Fermi levels in the contact leads and either the N-electron ground state (GS) (two lower lines) or the (N + 1)-electron GS (two upper lines). Located above and parallel to each upper line we observe dark lines (indicated by arrows), corresponding to alignment of one of the Fermi levels in the leads and the (N + 1)-electron excited state (ES). The excitation energy increases linearly with B. We therefore assign this ES as a Zeeman ES.

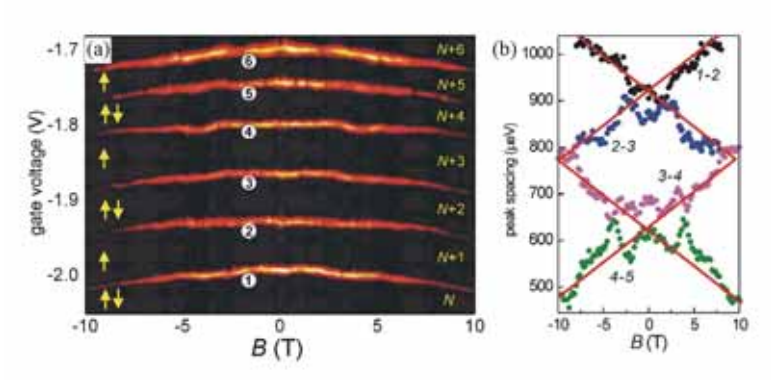

FIGURE 3. (a) Source-drain current I vs. V_g and B (V_{sd} = 30 μV, T = 70 mK) in a separate wire type device. The bright lines correspond to Coulomb peaks, the dark regions to Coulomb blockade. Spin orientations (arrows) are derived from the B-dependence of the Coulomb peak spacings. (b) Four successive Coulomb peak spacings (with offsets) vs. B. Points correspond to the Coulomb peak spacings. Solid lines are linear fits with the same absolute slope from which the g-factor is estimated.

The Zeeman energy is derived for a series of magnetic fields from the energy spacing between the GS and the Zeeman ES at 4 positions in the *dI/dV* plot [11]. These data are plotted in Fig. 2d and are used for a linear fit (solid line) from which we derive $|g_{dot}| = 0.23 \pm 0.02$.

This *g*-factor is smaller than that of bulk GaAs ($|g_{GaAs}| = 0.44$), probably due to the effect of electron confinement and the influence of the $Al_{0.3}Ga_{0.7}As$ barriers (bulk *g*-factor +0.4). From an excitation spectrum measurement in a perpendicular magnetic field (not shown here) on a different device fabricated out of the same wafer, we also find $|g_{dot}| \sim 0.23$. This independent result supports the interpretation of the excited state in Figs. 2a-c as a Zeeman excited state.

A Zeeman ES is not observed for the Coulomb blockade diamonds holding $N - 1$ and $N + 1$ electrons. We do not observe lines below and parallel to the lower boundaries of the *N*-electron Coulomb diamond, which would correspond to an $(N - 1)$-electron excited state. Complicated by the fact that we do not know the absolute electron number and the precise spin states in this dot, it is not clear why we only observe a clearly resolved Zeeman splitting in one particular case.

We also briefly discuss an alternative (but less accurate) method to derive the *g*-factor, used in a second device. Figure 3a shows the linear-response Coulomb peaks (bright lines) evolving with parallel magnetic field *B* for a different device. All Coulomb peaks shift to more negative gate voltages for increasing *B*, probably due to confinement effects in the leads and/or dot. To compensate for this effect, we plot the four successive Coulomb peak spacings (in units of energy, with offsets) vs. *B* in Fig. 3b. The peak spacings alternately increase (spin-decreasing transition) and decrease (spin-increasing transition) with *B*, indicating anti-ferromagnetic filling for this particular series of dot levels [12]. We estimate the value for the*g*-factor of $|g_{dot}| \sim 0.25$ from the slopes ($\pm g_{dot}\mu B$). This result is consistent with that obtained from the Coulomb diamond measurements discussed above. Note that for this particular device we are able to resolve the Zeeman splitting in a number of levels, as opposed to the Coulomb diamond results described above.

1.3. High-frequency experiments

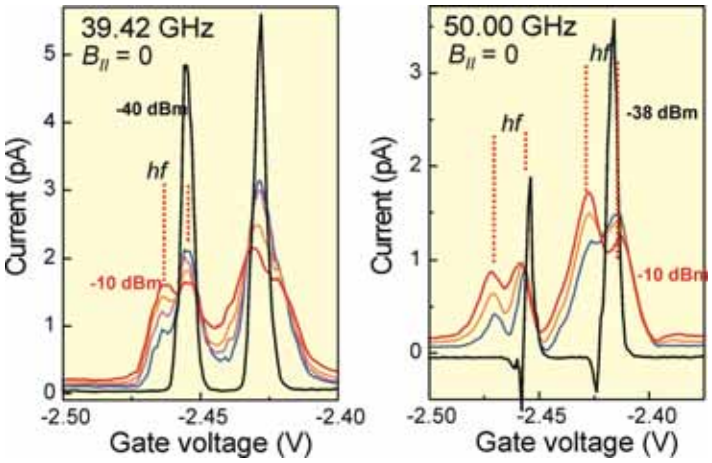

FIGURE 4. I-V_g plots at B = 0 for microwave powers from −40 to −10 dBm, f = 39.42 GHz (a) and from −38 to −10 dBm, f = 50 GHz (b). Satellite peaks ascribed to photon assisted tunneling are indicated.

Our microwave results indicate that instead of generating only an AC magnetic field, we also create a significant AC electric field near the dot, as illustrated by the data shown in Fig. 4 for two frequencies at $B_{//} = 0$. Here, we clearly see microwave induced satellite peaks (due to photon assisted tunneling) in combination with current rectification effects (photon assisted pumping) [13]. Since these phenomena do not show any resonant behavior as function of $B_{//}$, it should in principle be possible to separate them from the desired ESR-induced transport. We therefore apply a suitable microwave signal with frequency f and sweep $B_{//}$ around a field $B_{//,res}$ such that $|g_{dot}|\,\mu_B B_{//,res} = hf$. However, so far we have not been able to confirm ESR in our system, hampered by the effects described above and heating of the sample at larger microwave powers.
Our results confirm that microwave signals up to 50 GHz reach the sample, but more importantly, they indicate that we have to reduce the AC voltage generated in the dot and possibly also the heating of the sample. We are presently working on new devices with improved geometry and transmission line characteristics to meet these requirements.

1.4. Alternative approaches

To the best of our knowledge, so far there have been no reports on single electron spin resonance in semiconductor quantum dots. Single-spin rotation turns out to be a very challenging task. One of the main problems, separation of ac magnetic and electric fields, has been put forward above.

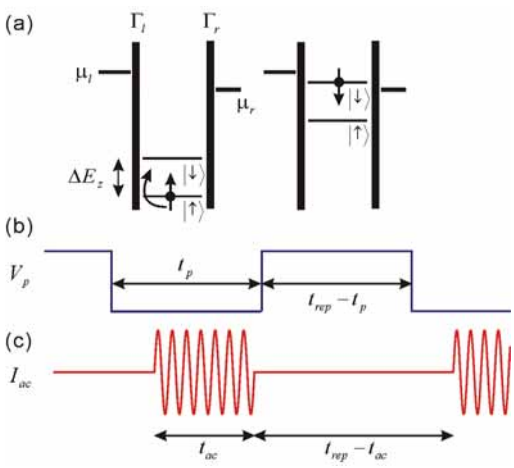

FIGURE 5. Pulse and probe measurement scheme for detecting single electron spin resonance in transport through a quantum dot. (a)

Schematic level diagrams showing the Zeeman split levels (Zeeman splitting ΔE_z) in two configurations. During the pulse time, t_p, a voltage pulse signal, V_p, is applied such that the levels are far below the fermi levels of the leads (left diagram). During this interval a microwave burst (length t_{ac}) is applied to the strip line causing an ac current, I_{ac}. The induced ac magnetic field leads to Rabi oscillations between the Zeeman split levels. After t_{ac}, the levels are brought positioned according to the configuration in the right diagram. Only if the electron is in the spin-down level, a contribution to the current is measured. (b) Voltage pulse signal with repetition time t_{rep}. (c) Ac current signal in the strip line.

A "pump and probe" scheme that should considerably reduce PAT and photon assisted pumping is schematically outlined in Fig. 5. A time-dependent voltage, $V_p(t)$ (Fig. 5b), is added to the dc gate voltage. $V_p(t)$ is a pulse signal that alternatively positions the Zeeman split dot levels far below the fermi levels of the leads (left diagram in Fig. 5), and the spin-down level above the fermi level of the right lead (right diagram in Fig. 5a). Instead of applying a continuous microwave signal to the ac line, bursts of microwave (Fig. 5c) are only applied to generate an ac magnetic field when the Zeeman split levels are in the lower position. Even when there is a finite ac electric field, the effect will be limited when ΔE_z is much smaller than the energy difference between the dot level and the fermi levels of the leads. As for PAT, only multi-photon processes could give rise to current. The probability of such processes strongly decreases for increasing photon number at small microwave powers [13]. Read-out is performed after turning off the microwave signal and pulsing up the Zeeman split levels.

Recently, Petta *et al.* demonstrated coherent control of a quantum two-level system (logical qubit) [5], based on two-electron spin states [14]. Rabi oscillations of these two-electron states are observed and, using quantum control techniques, a coherence time of more than 1 μs is found. It is shown time-ensemble-averaged dephasing time is limited by the hyperfine interaction with the spin-3/2 nuclei in the GaAs/AlGaAs host material. Although these results are very promising, single electron spin rotations have not been realized here either.

We have put forward another approach for realizing single-spin rotation, which is discussed in the next section.

2. Coherent single electron spin control in a slanting Zeeman field

We describe a general concept for realizing a solid-state quantum two-level system, based on a single electron in a quantum dot, which combines ease of manipulation with long coherence times [15]. This is accomplished by combining the spin and charge degrees of freedom of an electron in a quantum dot situated in a static slanting Zeeman field. A robust single pseudo-spin system is obtained that can be controlled by voltage only, without the need for an external time-dependent magnetic field or spin-orbit coupling. This unique and important feature is expected to considerably facilitate experimental realization of qubits based on single electrons. It is shown that both single qubit rotations and the C-NOT operation can be realized, thereby providing a universal set of gates for quantum computation. Using this approach it is also possible to determine the intrinsic single electron spin coherence time in the system.

An ac voltage is applied to let an electron in a QD oscillate under a *static* slanting Zeeman field. This effectively provides the electron spin with the necessary time-dependent magnetic field. Note the analogy with the Stern-Gerlach experiment, where the spin and orbital degrees of freedom are coupled by employing an inhomogenous magnetic field. The spatial oscillation of the electron within the QD involves the hybridization of orbital states, as schematically depicted in Fig. 6a for the case of the two lowest orbital states, $n = 1,2$.

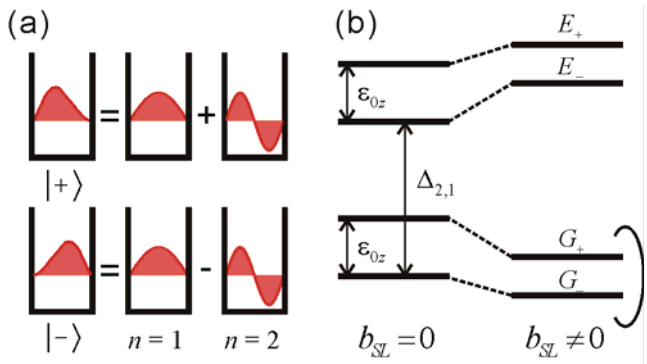

FIGURE 6. (a) Schematic representation of how a spatial oscillation between wavefunctions |+> and |−> involves hybridization of multiple orbital states. (b) Energy spectrum of a quantum dot (QD) with two orbital levels (level spacing $\Delta_{2,1}$) and constant Zeeman energy ε_{0z} with/without a magnetic field gradient b_{SL}. The lowest levels, $|G_\pm\rangle$, constitute a qubit. $|E_\pm\rangle$ are excited states.

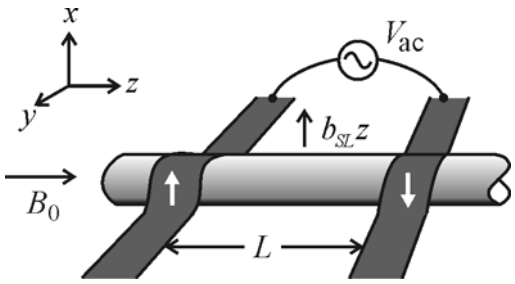

FIGURE 7. Model of the 1D QD in a slanting Zeeman field. Ferromagnetic gate electrodes (dark grey) are located at either end of the dot and are magnetically polarized in the plus/minus x-direction, creating a magnetic field gradient b_{SL}. A uniform magnetic field B_0 is applied in the z-direction. The spin in the dot is controlled by applying an oscillating voltage V_{ac} between the two gates.

Charge qubits based on double QDs [4] offer great tunability, but suffer from short coherence times (~1 ns) [16]. Spin qubits on the contrary, enable long coherence times (~1 μs) [5], but are much harder to control, as pointed out above. Here, we present a hybrid charge–spin system that is promising both in terms of tunability and coherence. Analogously, the combination of the flux and charge degrees of freedom has proved to be fruitful in superconducting qubits [17]. We stress that in our system spin–orbit (SO) coupling is not required, as opposed to earlier work on electron spin control based on *g*–tensor modulation [18], and on electric fields [19].

A possible realization of the system is presented in Fig. 7. A 1D conductor like a carbon nanotube or semiconductor nanowire is gated by ferromagnetic electrodes that define both the tunnel barriers of the QD and the slanting magnetic field. Alternatively, the slanting Zeeman field could be provided by a static inhomogeneity in the nuclear spin polarization or in the *g*–factor. The total magnetic field is given by $\boldsymbol{B} = b_{SL}z\boldsymbol{i}_x + (B_0+b_{SL}x)\boldsymbol{i}_z$, where B_0 is the external uniform magnetic field parallel to the *z*–axis and b_{SL} is the *z*–direction gradient of the field parallel to the *x*–axis (the middle of the QD corresponds to $z = 0$). A true 1D system is assumed with an electron strongly confined in the *x* and *y* directions. Therefore, the inhomogeneous term along the *z*–axis, $b_{SL}x\boldsymbol{i}_z$, can be eliminated (which is there to let $\boldsymbol{B}$ obey Maxwell's equations).

For the practical implementation of our scheme, 1D systems with small electron–phonon coupling and/or weak SO coupling are favorable. Single wall carbon nanotube QDs are very suitable, because of the absence of piezoelectricity and the weak deformation potential coupling [20]. SO coupling does not play a role either. QDs in semiconductor (e.g. SiGe) nanowires are also good candidates, since 1D phonons couple weakly to the electron orbitals. Here we estimate T_1 and Q of GaAs 1D QDs embedded in bulk AlGaAs. Since the phonon character is 3D in this system, the results are worse than for the more suitable systems given above. Figure 8a shows the low–temperature ($\beta\varepsilon_z \gg 1$) relaxation rate caused by bulk acoustic phonons in a QD with longitudinal parabolic confinement $\hbar\omega_0$ = 1 meV and a transversal confinement of 10 meV. E_{SL} = 1 μeV, corresponding to b_{SL} = 1.16

T/μm, which can be realized with a ferromagnetic material [21]. Of the three acoustic phonon scattering mechanisms, transversal piezoelectric scattering is dominant for low B_0, where T_1 is of the order of 10 ms. For comparison, the typical relaxation time from higher levels, i.e. $|E_\pm\rangle \rightarrow |G_\pm\rangle$ in Fig. 6b is much shorter, ~10 ns, dominated by the deformation potential scattering. Note that the contribution of SO interaction (Dresselhaus coupling) is very small ($T_{2SO} \sim 10^3$ s) in 1D QDs, in contrast to disk-shaped dots as examined in Ref. [22]. Figure 8b shows Q for various confinement potentials (dot length L) with b_{SL} = 1.16 T/μm. V_0 = 10 μV [13], and $t_\pi \sim$ 400 ns for $\hbar\omega_0$ = 1 meV. A quality factor $Q > 10^4$ is often used as a threshold for viable quantum computation [23].

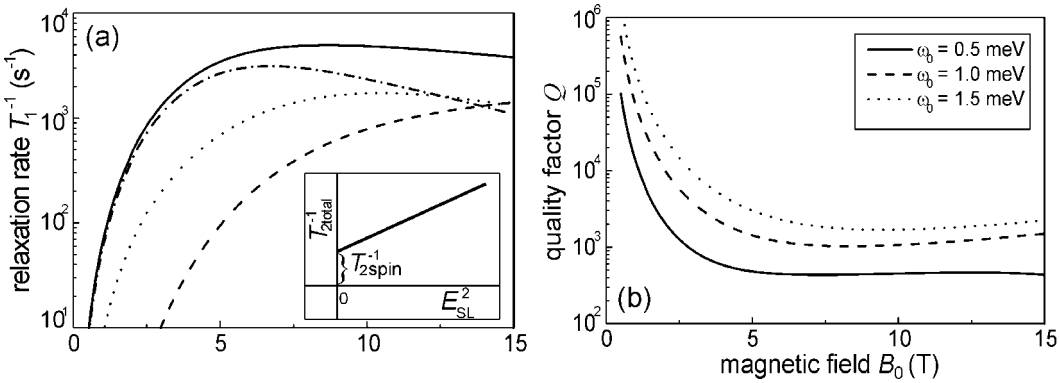

FIGURE 8. (a) Relaxation rate T_1^{-1} in a 1D GaAs QD as function of external magnetic field B_0 due to different phonon scattering mechanisms: deformation potential (dashed), longitudinal piezoelectric (dotted), transversal piezoelectric (dash-dotted). The solid line is the total scattering rate. Inset: schematic derivation of the pure electron spin coherence time T_{2spin} from the dependence of the total coherence time T_{2total} on the strength of the slanting field E_{SL}. (b) B_0-dependence of the quality factor Q for a single qubit p-operation.

For a universal set of quantum gates a two-qubit gate is required. Here we present a realization of a two-qubit gate based on two coupled dots in series [4]. Although it has been pointed out that an inhomogeneous magnetic field introduces swap errors [24], we show that correct swap operation is possible in our system, see Ref. [15].

3. Surface Acoustic Wave induced Transport in a Double Quantum Dot

3.1. Outline

We describe non-adiabatic transport through a double quantum dot under irradiation of surface acoustic waves generated on-chip. At low excitation powers, absorption and emission of single and multiple phonons is observed. At higher power, sequential phonon assisted tunneling processes excite the double dot in a highly non-equilibrium state. The present system is attractive for studying electron-phonon interaction with piezoelectric coupling.

3.2. Introduction

Electron-phonon coupling often leads to dissipation and decoherence problems in nanoelectronic devices. The decoherence in a tunable two-level quantum system (qubit), such as a double quantum dot (DQD) [4], is of particular interest in the recent light of quantum computation and information [25]. It was found that piezoelectric coupling to acoustic phonons is the dominant mechanism for inelastic transition between two charge states in a DQD [26], as confirmed by theory [27]. In analogy to quantum states in natural atoms – which dominantly couple to, and are successfully controlled by photons – the electronic states in solid state systems may be controlled by phonons, taking advantage of the strong electron-phonon coupling.

Due to the piezoelectric coupling in GaAs, surface acoustic waves (SAWs) can be generated by applying a microwave signal to an interdigital transducer (IDT) [28]. The accompanying propagating and oscillating potential

has been used in several experiments to transport photo-generated electrons and holes in so-called `dynamical quantum dots' [29]. In those experiments, however, the SAWs give rise to an adiabatic change of the electronic states, where the carriers remain in an eigenstate of the temporal potential.

In this section, we present *non-adiabatic* transitions in a lithographically defined DQD under irradiation of coherent SAWs. We observe resonant phonon assisted tunneling, where transport is well described by considering absorption and emission of one or multiple phonons during the tunneling process [30]. The present results unambiguously indicate a finite contribution of SAWs to the bosonic environment of a quantum two-level system formed by a DQD. Moreover, these transport measurements allow us to determine extremely small amplitudes of the local piezoelectric potential.

3.3. Device

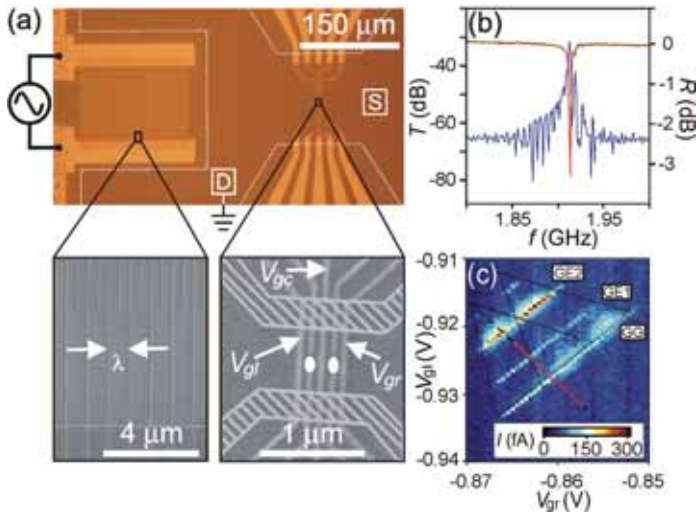

FIGURE 9. (a) Picture of the device with interdigital transducer (IDT, left) and double quantum dot (DQD, right). The source (S) and drain (D) reservoirs are indicated. The IDT-DQD distance is 227.5 µm. In the scanning electron micrograph (SEM) of the IDT, the electrodes, separated by λ = 1.4 µm, are visible. In the hatched regions of the DQD SEM the 2DEG is depleted by shallow dry etching. The position of the dots is indicated by white dots. (b) Transmission T (blue curve) and reflection R (red and greencurves) at room temperature of two IDTs similar to the one used in the experiments, separated by a distance of 455 µm. A clear peak in T and a dip in R are visible at 1.92 GHz. (c) Color scale plot of the DQD current as a function of gate voltages V_{gl} and V_{gr} at source drain voltage V_{SD} = 500 µV without SAW generation. The conductance triangles are accentuated by dotted lines. Resonant tunneling lines are clearly visible. The dual gate sweep direction for the SAW experiments is indicated by the red arrow.

Figure 9(a) is a picture of our device showing the Ti/Au gate patterns of the interdigital transducer used for generating SAWs on the left, and the DQD on the right on top of a GaAs/AlGaAs heterostructure with a 2Delectron gas (2DEG) 100 nm below the surface. The periodicity of the IDT is 1.4 µm, setting the SAW wavelength λ_{SAW}, and corresponding to a SAW frequency of about 2 GHz in GaAs [see lower left SEM micrograph in Fig. 9(a)]. The IDT design is characterized at room temperature using a different GaAs/AlGaAs heterostructure with two identical IDTs facing each other, allowing for a two-channel microwave measurement. The transmission and reflection spectra in Fig. 9(b) show a clear resonance at 1.92 GHz, as expected from the IDT design. The reflection dip is more than 3 dB, indicating that more than half of the incident power is absorbed in the IDT. The transmission reaches a maximum of −30 dB at resonance, implying additional loss in the device. Possible mechanisms for power loss are impedance mismatch, electromechanical conversion loss and Bragg reflection within the IDT. We found that the reflection and transmission spectra do not change when a DQD device is fabricated in the middle between the IDTs. By assuming identical characteristics for both IDTs, acoustic power at the site of the DQD is 15 dB less than the incident microwave power, *P*.

The DQD is formed in an etched channel of 600 nm width [see hatched dry etching regions in the lower right SEM micrograph in Fig. 9(a)] with appropriate voltages to the indicated gate electrodes, which have a 220 nm spacing [4].

3.4. Measurement results

All measurements described below, are performed in a dilution refrigerator with a base temperature of 50 mK. We have obtained similar results in two different samples, measured in different cryostats. The data shown here, are taken from one sample. Each dot contains ~10 electrons, has a charging energy of ~2 meV and a discrete energy level spacing of ~150 μeV. The inter-dot electrostatic coupling is ~200 μeV,
and the tunneling coupling is weak (<< 10 μeV) so that delocalization of states can be neglected. This weak coupling regime is suitable for studying electron-phonon interaction [26].

Figure 9(c) shows the single-electron tunneling current through the DQD versus gate voltages V_{gl} and V_{gr} with a large bias voltage of 500 μV with no microwave power (P = 0) applied to the IDT. The lower and upper (partly overlapping) triangular conduction regions correspond to electron-like and hole-like transport through the DQD, respectively [4]. Resonant tunneling through the ground states (GSs) of the two dots corresponds to the current peak at the base of the triangles (labeled GG), while other resonant tunneling between the left GS and the first and second excited states of the right dot are also observed (labeled GE1 and GE2). In the following measurements we simultaneously sweep V_{gl} and V_{gr} along the red arrow in Fig. 9(c), so that the energy difference $\Delta E = E_1 - E_2$ between the GS energies of the left dot (E_1) and the right dot (E_2) is varied. We observe a symmetric current profile around $\Delta E = 0$ representing elastic current through the DQD, while inelastic current at $\Delta E > 0$ associated with spontaneous emission of phonons is very small in the present experiment.

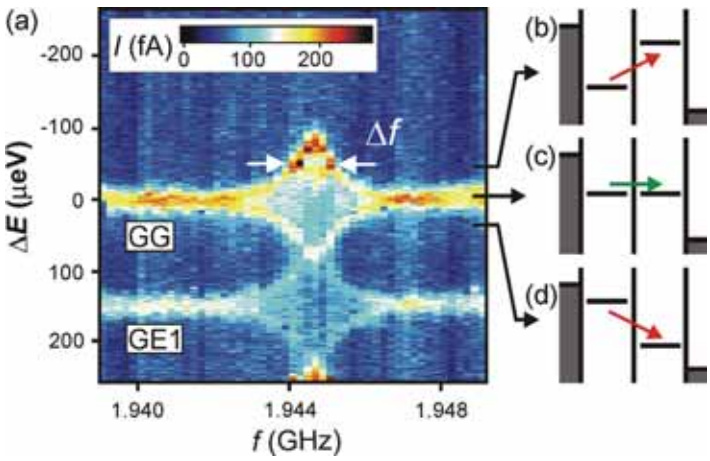

FIGURE 10. (a) Color scale plot of the DQD current versus ground state level spacing ΔE and microwave frequency f applied to the IDT (-40 dBm microwave power). V_{gl} and V_{gr} are swept along the red arrow indicated in Fig. 1(c). The current at ΔE=0 and 150 μeV corresponds to resonant tunneling through the ground states (GG), and through the left ground state and an excited state in the right dot (GE1), respectively. A clear resonance is observed at 1.9446 GHz (Δf = 1.4 MHz), corresponding to the IDT resonance frequency. The inelastic current is due to absorption and emission of SAW phonons, as schematically depicted in the energy diagrams (b) and (d), respectively. The energy diagram for elastic resonant tunneling is shown in (c).

When microwaves are applied to the IDT, we observe significant broadening and splitting of the resonant tunneling peaks only at the IDT resonant frequency, f_{SAW} = 1.9446 GHz, as seen in the frequency dependence of the current spectrum in Fig. 10(a). The resonance frequency corresponds very well to that of the GaAs reference sample (1.92 GHz) of Fig. 9(b), where the slight deviation is ascribed to the different heterostructure and the lower temperature in the actual device. This good correspondence rules out photon assisted tunneling [13]. There is no reason why there should be an electromagnetic resonance coinciding with the IDT resonance frequency. We also exclude resonant heating, since the energy levels are well separated from the Fermi levels of the leads. The harmonic

oscillation of the energy levels as described below, cannot be explained in terms of heating either. Note that no broadening is observed at off-resonant frequencies, also indicating that heating and spurious electromagnetic coupling are negligible.

We now look in more detail at the mechanism of the SAW-induced current in Fig. 10(a). The traveling SAW causes a time-dependent potential $V_{ac}\cos(2\pi f_{SAW}t)$ between the two quantum dots, due to the piezoelectric and deformation coupling. For GaAs at this frequency, the piezoelectric effect is dominant and the deformation coupling can be neglected [31]. As the lithographical dot-dot distance is d = 220 nm and the SAW wavelength is λ_{SAW} = 1.4 μm, V_{ac} is a fraction of the amplitude of the piezoelectric potential V_{pe}, $V_{ac} = \eta V_{pe}$, where $\eta = \sin(\pi d/\lambda_{SAW}) \approx 0.47$. The time-dependent level spacing $\Delta\widetilde{E}(t)$ is therefore $\Delta E + \eta V_{pe}\cos(2\pi f_{SAW}t)$. The peak splitting at resonance frequency in Fig. 10(a) can then be explained by a propagating SAW in the adiabatic limit as follows. Energy diagrams for positive ΔE, ΔE = 0, and negative ΔE are shown in Figs. 10(b), (c), and (d), respectively. Elastic current now appears at the time-dependent resonant condition $\Delta\widetilde{E}(t) = 0$. By assuming that the current is simply proportional to the time spent at resonant condition, current peaks appear at $\Delta E \pm \eta V_{pe}$ (i.e. at the classical turning points). The peak splitting is hence related to the piezoelectric potential amplitude.

The microwave power dependence of the current spectra is presented in Fig. 11(a). The peak splitting clearly increases with microwave power P. In Fig. 11(d) the splitting is plotted (black dots) as function of the amplitude of the microwave voltage applied to the IDT, V_{IDT}, confirming the linear dependence.

Since the tunneling rate (about 1 MHz for 100 fA current in our weakly-coupled DQD) is much smaller than f_{SAW}, an electronic state in one dot acquires a phase, which is given by the integration of the oscillating potential, relative to another state in the other dot [32]. This non-adiabatic effect appears for example as photon assisted tunneling, as evidenced in various devices under microwave or far-infrared irradiation [13]. In our case, the oscillating potential is obviously induced by *phonons*. One can say that the DQD is exposed to surface acoustic phonons with energy hf_{SAW} = 8 μeV. The energy-dependent tunnel rate $\widetilde{\Gamma}(E)$ from the left dot to the right dot in the presence of the phonon field is given by the same theory [4,32]

$$\widetilde{\Gamma}(\Delta E) = \sum_{n=-\infty}^{\infty} J_n^2(\alpha)\Gamma(\Delta E + nhf_{SAW}) \tag{1}$$

where n = 0, ±1, ±2,... is the number of phonons involved in the emission (positive n) and absorption (negative n), Γ(E) is the tunnel rate without phonons and $J_n^2(\alpha)$ is the squared n-th order Bessel function of the first kind evaluated at normalized amplitude $\alpha = eV_{ac}/hf_{SAW}$ [see inset to Fig. 11(c)]. The modulated DQD current $\widetilde{I}$ then becomes [30]

$$\widetilde{I} = e\,|t_{12}|\,\Gamma_R \sum_{n=-\infty}^{\infty} \frac{J_n^2(\alpha)}{\Gamma_R^2/4 + (n2\pi f_{SAW} - \Delta E/h)^2} \tag{2}$$

where $|t_{12}|$ is the modulus of the tunnel coupling between the two dots, and Γ_R the tunnel rate from the right dot to the right lead. Inelastic current is allowed whenever the level spacing equals an integer number times the phonon energy, i.e. $\Delta E = nhf_{SAW}$. The current thus consists of a number of satellite peaks, separated by the phonon energy hf_{SAW}. The Bessel function describes the probability that an electron absorbs ($n > 0$) or emits ($n < 0$) n phonons. It should be noted that Eq. (2) approaches the adiabatic limit for $\alpha \gg 1$.

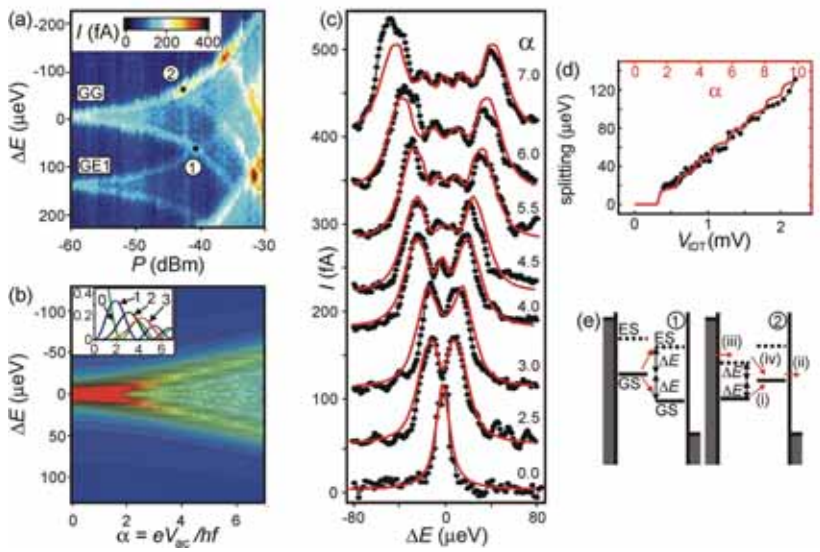

FIGURE 11. (a) Color scale plot of the DQD current versus ΔE and microwave power P, at f_{SAW}= 1.9446 GHz, for the same transitions as in Fig. 2. (b) Experimental (black dots) and calculated (red curves) current spectra for different microwave powers, extracted from (a) and (c), respectively. The experimental microwave power incident on the IDT is converted to normalized potential amplitude α using (d). The current height of the calculated spectra is fitted to the experimental data. (c) Calculated DQD current versus ΔE and α in the non-adiabatic limit, as explained in the text. Inset: squared Bessel functions $J_n^2(\alpha)$ for n = 0,1,2 and 3. (d) Splitting of the current peaks as function of the amplitude of the microwave voltage V_{IDT} applied to the IDT for the experimental data (black data points and axes), and current peak splitting derived from the calculated spectra in (c) as function of α (red curve and axes). By matching the experimental and calculated curves, the conversion between P and α is found. (e) Schematic energy level diagrams for the positions 1 and 2 indicated in (a). The transitions (i)-(iv) are discussed in the text.

Our DQD device has a resonant current line width of 14 μeV, even at zero microwave power, which is not sufficient to resolve phonon sideband with spacing hf_{SAW} = 8 μeV [33]. However, we do observe clear evidence of non-adiabatic effects in the current spectra, as described below. Figure 11(b) shows the DQD current as function of ΔE for different P. The lowest curve is measured at zero power and represents the elastic current. The fit of the elastic current, I_{el}, (red curve) is a Lorentzian with a FWHM of 14 μeV. The expected current at finite microwave power, $I_{SAW}(\Delta E)$, is now derived from the zero-power curve as $I_{SAW}(\Delta E) = \sum_{n=-\infty}^{\infty} J_n^2(\alpha) I_{el}(\Delta E + nhf_{SAW})$ and is plotted versus α in Fig. 11(c). For α ≳ 2 the resonant current splits in two peaks whose positions approach $\Delta E = \pm\alpha hf_{SAW}$, corresponding to the adiabatic limit. The splitting between the calculated current peaks versus α is plotted (red solid curve) together with the experimental splitting versus V_{IDT} in Fig. 11(d). Very good agreement between the experimental data and the non-adiabatic calculation is found when we relate V_{IDT} to the normalized ac potential α according to α = 0.09 $\eta e V_{IDT}/hf$. The first factor, corresponding to the loss in the IDT, is in good agreement with the loss estimated from Fig. 1b.

The non-adiabatic calculation in Fig. 11(c) shows clear additional structure in between the split peaks. This structure originates from the phonon satellite peaks that should be individually resolvable at $\Delta E = nhf_{SAW}$ if the peak width is smaller than the phonon energy. In our case, however, the peak width exceeds hf_{SAW} (but is less than $2hf_{SAW}$). We actually find good agreement between thecalculated current spectra and the experimental data (including the inter-peak fine structure) at finite microwave power as shown in Fig. 11(b), where we have applied the α-PdBm] conversion derived in Fig. 11(d). Our data thus reveal clear quantum behavior, even when we cannot resolve individual phonon satellites.

Quantum behavior is also observed in multiple excitation processes between excited states at higher power. As indicated by ① in Fig. 11(a), one of the split peaks of the GG resonance and one of the GE1 resonance touch around −40 dBm, where the GS-GS level spacing and the spacing between the GS in the left dot and the first ES in the right dot both equal V_{ac}, as shown in the left diagram of Fig. 11(e). At this condition, two phonon assisted tunneling processes (red arrows) are allowed from the GS of the left dot. There is another peak emerging for P >

−42 dBm indicated by ② in Fig. 11(a). This peak is associated with phonon assisted tunneling from an ES in the left dot to the GS of the right dot [right diagram of Fig. 11(e)]. This tunneling process is only possible if an electron first tunnels from the GS of the left dot to the GS of the right dot (i) and escapes to the right lead (ii), another electron tunnels into the ES of the left dot (iii) followed by tunneling to the GS of the right dot under phonon emission (iv). This explanation is consistent with the absence of the peak at lower power, where the GS in the left dot is permanently occupied. At higher power, more resonant peaks are resolved, which may be useful in analyzing the energy spectrum of our DQD.

Finally, we comment on the measurement sensitivity to the piezoelectric potential in our experiment. As discussed above, the current spectra reflect the amplitude of the local piezoelectric potential. The lowest power at which we can resolve peak splitting is −58 dBm, corresponding to V_{pe} = 24 μV, which is several orders of magnitude smaller than the power used to induce dynamical quantum dots [29] and to induce lattice displacements measurable by optical interferometry [34]. The minimum detection power can be improved further by adjusting the DQD parameters. When the elastic current peak width is made smaller than the phonon energy, the piezoelectric potential can be derived from the amplitude of the phonon assisted tunneling current via the Bessel function dependence even for $\alpha \ll 1$. This may enable the measurement of lattice distortion due to vacuum fluctuations.

3.5 Conclusion

In conclusion, we have observed inelastic tunneling in a DQD two-level system coupled to a monochromatic SAW source. The transport through the DQD is well described by non-adiabatic Tien-Gordon theory for resonant tunneling between two discrete states with a time-dependent potential. We find that the DQD can be employed as a very sensitive SAW detector and is promising for studying electron-phonon interaction.

References

[1] See, for example, M. A. Nielsen and I. L. Chuang, Quantum Computation and Quantum Information, (Cambridge University Press, Cambridge, 2001).

[2] D. Loss and D.P. DiVincenzo, Phys. Rev. A **57**, 120 (1998).

[3] L.P. Kouwenhoven, C.M. Marcus, P.L. McEuen, S. Tarucha, R.M. Westervelt and N.S. Wingreen, *Electron transport in quantum dots, in Mesoscopic Electron Transport*, edited by L.L. Sohn, L.P. Kouwenhoven and G. Schon, (Kluwer, Series E **345**, 1997), p.105-214.

[4] W. G. van der Wiel, S. De Franceschi, J. M. Elzerman T. Fujisawa, S. Tarucha and L. P. Kouwenhoven, Rev. Mod. Phys. **75**, 1 (2003).

[5] J.R. Petta, A.C. Johnson, J.M. Taylor, E.A. Laird, A. Yacoby, M.D. Lukin, C.M. Marcus, M.P. Hanson, A.C. Gossard, Science **309**, 2180 (2005).

[6] H.A. Engel and D. Loss, Phys. Rev. Lett. **86**, 4648 (2001).

[7] H.A. Engel and D. Loss, Phys. Rev. B **65**, 195321 (2002).

[8] J.M. Elzerman, R. Hanson, L.H. Willems van Beveren, B. Witkamp, L.M.K. Vandersypen and L.P. Kouwenhoven, Nature **430**, 431 (2004).

[9] S. Tarucha, D. G. Austing, T. Honda, R. J. van der Hage, L. P. Kouwenhoven, Phys. Rev. Lett. **77**, 3613 (1996).

[10] T. Kodera, W.G. van der Wiel, K. Ono, S. Sasaki, T. Fujisawa and S. Tarucha, Physica E **22**, 518 (2004).

[11] T. Kodera, W.G. van der Wiel, T. Maruyama, Y. Hirayama and S. Tarucha, in *Realizing controllable quantum states*, H. Takayanagi, J. Nitta (eds.), pp. 445-450, World Scientific Publishing, Singapore (2005).

[12] R.M. Potok, J.A. Folk, C.M. Marcus, V. Umansky, M. Hanson and A.C. Gossard, Phys. Rev. Lett. **91**, 016802, (2003).

[13] W.G. van der Wiel, *et al.*, Photon assisted tunneling in quantum dots in *Strongly Correlated Fermions and Bosons in Low-Dimensional Disordered Systems*, eds. I.V. Lerner *et al.*, pp.43-68, Kluwer Academic Publishers (2002).

[14] J. Levy, Phys. Rev. Lett. **89**, 147902 (2002).

[15] Y. Tokura, W.G. van der Wiel, T. Obata and S. Tarucha, accepted for publication in Phys. Rev. Lett.; cond-mat/0510411 (2005).

[16] T. Hayashi *et al.*, Phys. Rev. Lett. **91** 226804 (2003).

[17] D. Vion *et al.*, Science **296**, 886 (2002).

[18] Y. Kato *et al.*, Science **299**, 1201 (2003).

[19] E.I. Rashba and Al. L. Efros, Phys. Rev. Lett. **91**, 126405 (2003).

[20] H. Suzuura and T. Ando, Phys. Rev. B **65**, 235412 (2002).
[21] J. Wrobel *et al.*, Phys. Rev. Lett. **93**, 246601 (2004).
[22] A.V. Khaetskii and Yu.V. Nazarov, Phys. Rev. B **64**, 125316 (2001).
[23] A.M. Steane, quant-ph/0207119 and references therein.
[24] R. de Sousa, X. Hu, and S. Das Sarma, Phys. Rev. B **64** 42307 (2001).
[25] A.J. Leggett *et al.*, Rev. Mod. Phys. **59**, 1 (1987).
[26] T. Fujisawa *et al.*, Science 282, 932 (1998); T. Fujisawa, W.G. van der Wiel and L.P. Kouwenhoven, Physica E **7**, 413 (2000).
[27] T. Brandes and B. Kramer, Phys. Rev. Lett. **83**, 3021 (1999).
[28] A.A. Oliner, *Acoustic Surface Waves*, Springer-Verslag, Berlin Heidelberg, Germany (1978).
[29] C.H.W. Barnes *et al.*, Phys. Rev. B **62**, 8410 (2000); J.A.H. Stotz *et al.*,, Nat. Mat. **4**, 585 (2005).
[30] T.H. Stoof and Yu.V. Nazarov, Phys. Rev. B **53**, 1050 (1996).
[31] P.V. Santos, private communication.
[32] P.K. Tien and J.R. Gordon, Phys. Rev. **129**, 647 (1963).
[33] This width is most probably due to charge instability in the heterostructure we used.
[34] M.M. de Lima *et al.*, J. Appl. Phys. **94**, 7848 (2003).

今後の展開 (Future Plan)

Single-electron ESR has turned out to be an extremely difficult task. Although many groups world-wide put a lot of effort in realizing this goal, no one has succeeded so far in demonstrating single-electron ESR in a semiconductor quantum dot. Prof. Tarucha's group will continue working on the application of semiconductor few-electron dots as quantum bits and also on the realization of single-electron ESR. In particular, we use the scheme of coherent single electron spin control in a slanting Zeeman field, as outlined in section 4.2. This approach may be more successful than the generation of an ESR field by an ac current.

The study of surface acoustic wave induced transport in a double quantum dot has been very successful and has given interesting results on electron-phonon interaction. The interaction between a solid-state qubit and phonons in the environment is very relevant for the coherence time. This line of research will therefore be continued at NTT Basic Research Labs. in the group of Dr. Fujisawa. In particular, the interaction between a double quantum dot and a phonon cavity is envisioned as a follow-up experiment.

At the University of Twente, I will continue working myself in the field of spintronics as well. One of my project will focus on spin transport in organic materials. The spin relaxation time in organic materials should be extremely long due to small spin-orbit coupling and weak hyperfine interaction. This could open up the possibility of coherent spin manipulation in such systems.

研究成果リスト (List of Publication)

（1）論文（原著論文）(Original Articles)

in preparation:

11. **Surface acoustic wave induced transport in a double quantum dot**
W.J.M. Naber, T. Fujisawa, H.W. Liu and W.G. van der Wiel
submitted to Physical Review Letters; cond-mat/0601158 (2006).

10. **Semiconductor quantum dots for electron spin qubits**
W.G. van der Wiel, M. Stopa, T. Kodera, T. Hatano and S. Tarucha
submitted to the New Journal of Physics (2005).

09. **Coherent single electron spin control in a slanting Zeeman field**
Y. Tokura, W.G. van der Wiel, T. Obata and S. Tarucha

Physical Review Letters, in press; cond-mat/0510411 (2005).

published

08. **Kondo effects in quantum dots**
S. Tarucha, S. Sasaki and W.G. van der Wiel
Journal of the Physical Society of Japan **60-2**, 110-118 (2005).

07. **Fabrication and characterization of quantum dot single electronspin resonance devices**
T. Kodera, W.G. van der Wiel, T. Maruyama, Y. Hirayama and
S. Tarucha, in *Realizing controllable quantum states*, H. Takayanagi, J. Nitta (eds.), pp. 445-450, World Scientific Publishing, Singapore (2005).

06. **Electron spin redistribution in a Kondo quantum dot in the low-magnetic-field regime**
W.G. van der Wiel, M. Stopa, S. De Franceschi, L.P. Kouwenhoven and
S. Tarucha
Physica E **22**, 538 (2004).

05. **High-frequency manipulation of few-electron double quantum dotstoward spin qubits –**
T. Kodera, W.G. van der Wiel, K. Ono, S. Sasaki, T. Fujisawa and S. Tarucha
Physica E **22**, 518 (2004).

04. **Magnetically Induced Chessboard Pattern in the Conductance of a Kondo Quantum Dot**
M. Stopa, W.G. van der Wiel, S. De Franceschi, S. Tarucha and
L.P. Kouwenhoven
Phys. Rev. Lett. **91**, 046601 (2003).

03. **Interactions, Spins and the Kondo Effect in Quantum-Dot Systems**
S. Tarucha, K. Ono, T. Fujisawa, W.G. van der Wiel and L.P. Kouwenhoven
in *Electron Transport in Quantum dots*, J.P. Bird (ed.), pp. 1-42,
Kluwer Academic Publishers Boston/Dordrecht/London (2003).

02. **Electro-magnetic Aharonov-Bohm effect in a 2-D electron gas ring**
W.G. van der Wiel, Yu.V. Nazarov, S. De Franceschi, T. Fujisawa,
J.M. Elzerman, E.W.G.M. Huizeling, S. Tarucha and L.P. Kouwenhoven
Phys. Rev. B **67**, 033307 (2003).

01. **Electron transport through double quantum dots**
W.G. van der Wiel, S. De Franceschi, J.M. Elzerman, T. Fujisawa,
S. Tarucha and L.P. Kouwenhoven
Rev. Mod. Phys. **75**, 1 (2003).

発表 (Oral Presentations)

15. **Electron charge and spin in semiconductor quantum dots (invited)**
37th Conference of the European Group for Atomic Systems (EGAS37), Dublin, Ireland,

3-6 August 2005

14. **Surface acoustic wave induced transport in double quantum dots (invited seminar)**
Paul-Drude-Institut für Festkörperlektronik, Berlin, Germany, 1 July 2005

13. **Phonon assisted transport in double quantum dots and phonon focusing (invited seminar)**
Institut für Festkörperforschung (IFF) Kolloquium, Forschungszentrum Jülich, Germany, 10 June 2005

12. **Electron spin qubits and phonon assisted transport in semiconductor quantum dots (invited seminar)**
University of California, Los Angeles, 4 March 2005

11. **Electron spin qubits in semiconductor quantum dots (invited seminar)**
Stanford University, USA, 15 November 2004

10. **Quantum computation using electron spins in semiconductor quantum dots (invited)**
42nd Kaya Conference, Zaou, Japan, 22-25 August 2004

09. **Electron-spin manipulation in vertical quantum dots – experimental progress –**
International Symposium on Mesoscopic Superconductivity and Spintronics 2004 (MS+S2004), NTT R&D Center, Atsugi, Japan March 1-4, 2004

08. **Microwave electron-spin manipulation in vertical quantum dots**
Solid State Quantum Information Processing Conference(SSQIP), Amsterdam, The Netherlands, 15-18 December 2003

07. **Electron transport experiments in semiconductor quantum dots (invited)**
International Summer School for Young Researchers on Quantum Transport in Mesoscopic Scale & Low Dimensions, Kashiwa, Japan, 13-21 August 2003

06. **Kondo chessboard pattern in the conduction of a quantum dot**
15th International Conference on the Electronic Properties of Two-Dimensional Systems (EP2DS-15), Nara, Japan, 14-18 July 2003

05. **Microwave manipulation of few-electron quantum dots**
Frontiers of Nanoscale Science and Technology, Jointly organized by the Nanoscale Science and Engineering Center and the University of Tokyo, University of Tokyo, 10-12 July 2003

04. **High-frequency single-electron spin manipulation in semiconductor quantum dots**
Gordon Research Conferences, Quantum Information Science, Ventura, California, USA 23-28, March 2003

03. **Coherent electron spin phenomena in quantum dots (invited seminar)**
Stanford University, USA, 20 March 2003

02. **Single-electron spin manipulation in quantum dots**
Carrier Interactions and Spintronics in Nanostructures (CISN2003), NTT Atsugi R&D center, Japan, March 10-12, 2003

01. **Microwave electron spin manipulation in semiconductor artificial atoms and molecules**
PASPS8, The 8th Symposium on the Physics and Application of Spin Related Phenomena in Semiconductors, Sendai, Japan, 19-20 December 2002

（2）特許出願（Patent Application）
なし（None）

（3）その他の成果（Others）
2005　chair of the 2005 Gordon Research Conference on Quantum Information Science, Ventura CA, USA
2005　chair of the 2005 MESA+ meeting, Enschede, The Netherlands